Communications Physics

https://doi.org/10.1038/s42005-026-02799-x

Article in Press

Sign-engineered interactions enable dynamic frustration and topology in a passive elastic lattice

Received: 30 April 2026

Accepted: 24 July 2026

Published online: 03 August 2026

Cite this article as: Lee, T., Yu, Z., Su, X. *et al.* Sign-engineered interactions enable dynamic frustration and topology in a passive elastic lattice. *Commun Phys* (2026). https://doi.org/10.1038/s42005-026-02799-x

Taehwa Lee, Ziqi Yu, Xiaoshi Su, Hyung-Suk Kwon & Chiara Daraio

We are providing an unedited version of this manuscript to give early access to its findings. Before final publication, the manuscript will undergo further editing. Please note there may be errors present which affect the content, and all legal disclaimers apply.

If this paper is publishing under a Transparent Peer Review model then Peer Review reports will publish with the final article.

ARTICLE IN PRESS

© The Author(s) 2026. **Open Access** This article is licensed under a Creative Commons Attribution-NonCommercial-NoDerivatives 4.0 International License, which permits any non-commercial use, sharing, distribution and reproduction in any medium or format, as long as you give appropriate credit to the original author(s) and the source, provide a link to the Creative Commons licence, and indicate if you modified the licensed material. You do not have permission under this licence to share adapted material derived from this article or parts of it. The images or other third party material in this article are included in the article's Creative Commons licence, unless indicated otherwise in a credit line to the material. If material is not included in the article's Creative Commons licence and your intended use is not permitted by statutory regulation or exceeds the permitted use, you will need to obtain permission directly from the copyright holder. To view a copy of this licence, visit http://creativecommons.org/licenses/by-nc-nd/4.0/.

ARTICLE IN PRESS

Sign-Engineered Interactions Enable Dynamic Frustration and Topology in a Passive Elastic Lattice

Taehwa Lee[1] [*], Ziqi Yu[1], Xiaoshi Su[1], Hyung-Suk Kwon[1], Chiara Daraio[2] [†]

[1]Toyota Research Institute of North America, Toyota Motor North America, Ann Arbor, Michigan 48105, USA

[2]Division of Engineering and Applied Science, California Institute of Technology, Pasadena, California 91125, USA

ARTICLE IN PRESS

Abstract

The sign and strength of interactions between coupled elements govern collective phenomena ranging from wave localization to topological phases and frustration. Whereas active systems can tune interaction signs through external driving, passive systems are typically limited to fixed structures where reversing signs requires changes to lattice connectivity or global symmetry. Here we demonstrate, both theoretically and experimentally, that local anisotropy enables continuous Hamiltonian sign engineering in central-force elastic lattices. Rotating anisotropic confinement projects interactions onto local degrees of freedom, decomposing the two-dimensional dynamics into spectrally separated one-dimensional Hamiltonians with continuously tunable effective couplings—from positive to negative—via rotation alone, without altering the force law or lattice connectivity. Implemented in a zigzag magnetoelastic lattice, this mechanism enables the concurrent emergence of frequency-selective wave frustration and topological band inversion in a single passive system. These results establish local anisotropy as a general tool for Hamiltonian engineering and offer a classical analogue to phonon-mediated interaction design in quantum many-body platforms.

[*]Correspondence to: taehwa.lee@toyota.com
[†]Correspondence to: daraio@caltech.edu

ARTICLE IN PRESS

Introduction

Interactions between coupled elements govern a wide range of collective phenomena, from wave propagation and localization to topological phases [1, 2] and frustration [3, 4]. In engineered lattices, interaction strength can often be tuned geometrically, enabling nonlocal coupling [5–7], band inversion [8], and topological states [9, 10]. In contrast, the sign of the interaction—whether neighboring elements favor in-phase or out-of-phase motion—is typically fixed by the underlying force law. Control over interaction sign is particularly consequential [11], as reversing the coupling sign alters dispersion curvature, band ordering, and the emergence of competing interactions underlying frustrated many-body states [3, 4, 12, 13].

The ability to control interaction signs is thus fundamental to the realization of programmable synthetic Hamiltonians. Programmable quantum platforms, such as trapped ions [14, 15] and Rydberg atom arrays [16, 17], achieve this through active modulation and external driving, enabling simulation of complex spin models with tunable couplings. In classical systems, however, existing approaches to sign control are similarly dependent on active modulation or platform-specific mechanisms, including feedback-controlled non-Newtonian metamaterials [18, 19], spatiotemporal modulation [20], and synthetic gauge-field engineering [21]. Although passive strategies have been explored through discrete parity engineering [22], constraint-based mode projection [9, 23], and orbital mixing [24], a general passive framework for continuous sign control has not yet been established.

Here we demonstrate local anisotropy as a universal mechanism for Hamiltonian sign engineering in central-force elastic lattices. By projecting the longitudinal and transverse components of a central interaction onto rotated local degrees of freedom, we demonstrate that the system's dynamics can be decomposed into spectrally separated, one-dimensional Hamiltonians. Within each reduced Hamiltonian, the effective coupling is continuously tunable from positive to negative through a simple rotation of the anisotropy axes—requiring no modifications to the underlying force law or lattice connectivity. We implement this principle in a magnetoelastic zigzag lattice, revealing that the projected Hamiltonian admits a dual description that bridges Su-Schrieffer-Heeger (SSH)-type band topology and XY-type phase interactions within the same architecture. Furthermore, we experimentally show that this mechanism enables the coexistence of topology and frustration in a purely static framework. These results provide a general platform for interaction engineering in wave systems and offer a powerful classical analogue to the phonon-mediated Hamiltonian design relevant to quantum many-body platforms.

ARTICLE IN PRESS

Results and discussion

Sign-tunable Hamiltonians via local anisotropy

We consider a central-force elastic lattice subject to locally anisotropic confinement, as illustrated in Fig. 1(a). The quadratic trapping potential $V = \frac{1}{2}k_a a^2 + \frac{1}{2}k_b b^2$ defines two orthogonal local axes ($\vec{\mathbf{a}} \perp \vec{\mathbf{b}}$) with stiffnesses $k_a < k_b$. Rotating this potential by an angle θ_c yields the local stiffness matrix $\mathbf{K}_i(\theta_c) = \mathbf{R}(\theta_c)\mathrm{diag}(k_a, k_b)\mathbf{R}^{\mathrm{T}}(\theta_c)$. The total Hamiltonian of the system is expressed as

$$H = \sum_i \left(\frac{\mathbf{p}_i^{\mathrm{T}}\mathbf{p}_i}{2m} + \frac{1}{2}\mathbf{u}_i^{\mathrm{T}}\mathbf{K}_i\mathbf{u}_i \right) + \sum_{\langle i,j \rangle} \mathbf{E}_{ij}, \tag{1}$$

where $\mathbf{p}_i$ and $\mathbf{u}_i$ are the momentum and displacement vectors at site i, and $\mathbf{E}_{ij}$ represents the interaction energy between neighboring sites j and i.

The interaction energy $\mathbf{E}_{ij}$ depends entirely on a spatially homogeneous, constant underlying connectivity. These bond-based interactions are characterized by longitudinal ($k_\parallel$) and transverse ($k_\perp$) stiffnesses acting parallel and perpendicular to the unit bond vector $\mathbf{d}_{ij}$, respectively. Following the dynamical matrix formulation for oscillator networks [25], the interaction energy is given by

$$\mathbf{E}_{ij} = \frac{1}{2}(\mathbf{u}_i - \mathbf{u}_j)^{\mathrm{T}}\mathbf{M}_{ij}(\mathbf{u}_i - \mathbf{u}_j), \tag{2}$$

where $\mathbf{M}_{ij} = k_\parallel \mathbf{P}_{ij}^\parallel + k_\perp \mathbf{P}_{ij}^\perp$ represents the interaction stiffness matrix. Here, the projection operators, $\mathbf{P}_{ij}^\parallel = \mathbf{d}_{ij}\mathbf{d}_{ij}^{\mathrm{T}}$ and $\mathbf{P}_{ij}^\perp = \mathbf{I} - \mathbf{d}_{ij}\mathbf{d}_{ij}^{\mathrm{T}}$, decompose the displacement differences into their respective bond components.

To achieve continuous Hamiltonian engineering, we exploit the strong-anisotropy limit $k_a \ll k_b$. In this regime, the system Hamiltonian decomposes into spectrally separated 1D Hamiltonians ($H \approx H_a \oplus H_b$) as the inter-manifold coupling H_{ab} vanishes (Fig. 1(a)). This separation provides a classical analogue of Hilbert space reduction via Schrieffer-Wolff transformation [26].

Projecting the bond interactions onto the local soft axis $\vec{\mathbf{a}}$ yields the effective 1D coupling for the low-frequency manifold H_a (see Method) [27]

$$k_{\mathrm{eff}}^{(a)}(\alpha) = k_\perp + (k_\parallel - k_\perp)(\mathbf{d}_{ij} \cdot \vec{\mathbf{a}})^2, \tag{3}$$

where α is the projection angle between the bond direction $\mathbf{d}_{ij}$ and the soft axis $\vec{\mathbf{a}}$ ($\mathbf{d}_{ij} \cdot \vec{\mathbf{a}} = \cos\alpha$). This mechanism enables continuous tuning of $k_{\mathrm{eff}}^{(a)}$ between $k_\parallel$ and $k_\perp$ (Fig. 1(b)).

Such control is inherent to physical systems with nonlinear central forces $F(d) = Ad^p$ (e.g., dipolar $p = -4$ or Coulomb $p = -2$ interactions). Linearizing about a prestressed equilibrium d_0 yields $k_\parallel = pk_\perp$, where $p < 0$ ensures that $k_\parallel$ and $k_\perp$ possess opposite signs ($k_\perp < 0 < k_\parallel$). Consequently, rotating the anisotropy axis enables absolute sign control over the interaction. As demonstrated in a two-mass system (Fig. 1(b), bottom), negative coupling inverts the fundamental mode ordering: the antisymmetric mode (f_{AS}) appears at a lower frequency than the in-phase mode

ARTICLE IN PRESS

(f_S), a direct reversal of conventional lattice behavior (Supplementary Note 1, Fig. S1).

Programmable dispersion and manifold isolation in zigzag lattices

The robust manifold separation established above allows the lattice to preserve full two-dimensional dynamics while operating within spectrally isolated projected subspaces. Figure 2(a) shows the dispersion spectrum of an infinite periodic zigzag lattice as a function of the anisotropy angle θ_c. Two distinct mode groups are observed: the lower-frequency a-manifold (H_a) and the higher-frequency b-manifold (H_b), separated by a wide spectral gap induced by the high local stiffness ratio ($k_b/k_a \approx 12$). To quantify the isolation, we define a mode polarization parameter P_a, where $P_a = 1$ (red) denotes a pure a-manifold mode and $P_a = 0$ (blue) a pure b-manifold mode. The sharp color contrast in Fig. 2(a) confirms negligible cross-manifold mixing, validating the $H \approx H_a \oplus H_b$ decomposition (Supplementary Note 2, Fig. S2).

Synthetic interactions within these manifolds are programmed by reconfiguring the local anisotropy angle θ_c, which simultaneously modulates the magnitude and sign of nearest-neighbor (intra and inter) and long-range (LR) couplings (Fig. 2(b)). In the zigzag geometry, defined by identical bond lengths and an inter-bond angle of $\theta = \pi/3$, the projection angles are bond-specific ($\alpha = \theta \pm \theta_c$ or θ_c), inducing inhomogeneous effective stiffnesses. A key feature of this platform is that the effective coupling k_{eff} for the a-manifold is shifted by 90° relative to that of the b-manifold. This orthogonality allows the same lattice to realize disparate interaction signs and strengths across manifolds, such that $k_{\text{eff}}^{(a)}(\theta_c) \neq k_{\text{eff}}^{(b)}(\theta_c)$. Consequently, the lattice can behave as a topological insulator in one manifold while remaining a trivial phase in the other.

Representative configurations ($\theta_c = 0, 30, 50, 70, 90°$) are illustrated in Fig. 2(c), enabling the diverse combinations of bond signs and strengths accessible within a single lattice. At $\theta_c = 0°$, the lattice exhibits dominant nonlocal horizontal coupling. Moving toward 70°, the lattice shows dimerization along the zigzag line. Finally, at $\theta_c = 90°$, negative long-range interactions emerge. As evidenced in the a-manifold dispersion evolution (lower panel), varying θ_c transitions the system through distinct physical regimes (see Supplementary Note 3, Fig. S3). These results demonstrate that local anisotropy rotation acts as a control knob for programming the synthetic Hamiltonians of elastic metamaterials.

Frequency-selective wave frustration and topological coexistence

To demonstrate the power of sign control, we focus on sign-conflict-induced wave frustration, inaccessible in conventional lattices with purely positive couplings. Unlike geometric frustration in static systems, where incompatible interactions constrain equilibrium configurations [3, 4], the frustration here is inherently dynamical, emerging from wave propagation governed by projection-controlled coupling signs. This mechanism is distinct from flat-band physics in kagome lattices [28, 29], where phase conflict arises solely from phase accumulation along closed paths rather than intrinsic sign incompatibility.

ARTICLE IN PRESS

As illustrated in Fig. 3, an odd number of negative couplings in a closed loop ($\Phi < 0$) enforces incompatible phase relations between neighboring oscillators. At low wavenumber (q_{LOW}), negative couplings favor out-of-phase motion while positive couplings favor in-phase motion, producing an irresolvable phase loop. At high wavenumber, the phase configuration becomes compatible and frustration is relieved. This wavenumber dependence follows from the time-averaged XY-like Hamiltonian [30],

$$\langle H_{ij}^{\mathrm{corr}} \rangle = -k_{\mathrm{eff}}(\alpha) A_i A_j \cos(\Delta\phi) \tag{4}$$

where $\Delta\phi = \phi_i - \phi_j - qd$ includes path-dependent phase accumulation qd. Energy minimization requires $\Delta\phi = 0$ for $k_{\mathrm{eff}} > 0$ and $\Delta\phi = \pi$ for $k_{\mathrm{eff}} < 0$, depending on low ($qd \approx 0$) or high ($qd \approx \pi$) wavenumbers. The phase-correlation interpretation of oscillatory states yields the XY-like picture, while the linear eigenvalue problem yields the SSH-type band picture.

Figure 4(a) shows a frustrated zigzag lattice in a-manifold ($\Phi < 0$) and an ordinary lattice ($\Phi > 0$). The frustrated lattice is experimentally realized using a magnetoelastic zigzag array [31, 32] (Fig. 4(b)), where repulsive magnetic interactions ($F = Ad^p$, $p \approx -4.1$) provide central-force coupling ($k_\perp = -4.36$ N/m, $k_\parallel = 17.96$ N/m) and anisotropic cantilevers introduce strong stiffness contrast ($k_b/k_a \approx 12$), ensuring clear manifold separation. For cantilever tilting $\theta_c = 90°$, the long-range coupling becomes negative ($k_{\mathrm{LR}} < 0$) in the a-manifold, yielding a frustrated loop $\Phi = \mathrm{sign}(k_{\mathrm{inter}} k_{\mathrm{intra}} k_{\mathrm{LR}}) < 0$.

Figures 4(c) and 4(d) show theoretical and experimental dispersion relations in the a-manifold. The one-dimensional effective-coupling model (H_a) agrees with the full two-dimensional Jacobian-matrix model (H), again confirming projection-induced decomposition. A key frustration signature is the finite-q band minimum, distinct from roton-like dispersion with positive long-range couplings [33], leading to pronounced mode crowding near the band edge where eigenmodes accumulate within a narrow frequency band (Fig. 4(c), right panel). We verify this experimentally through the mode participation factor S_n (Fig. 4(d), right panel). At $f = 27$ Hz multiple modes contribute simultaneously, whereas at $f = 34$ Hz a single mode dominates. Within the crowding band, frustrated mode profiles exhibit oscillatory patterns even for the fundamental mode (Fig. 4(e)), reflecting accommodation of competing coupling signs, further confirmed by measured phase differences along horizontal bonds that favor π phase separation (Fig. 4(f)). The corresponding real-time dynamics are shown in Supplementary Videos 1, 2.

The frustration in the a-manifold persists for $60° < \theta_c < 120°$, but deviating from 90° introduces dimerization ($k_{\mathrm{inter}} \neq k_{\mathrm{intra}}$), triggering a topological transition described by the SSH model. This enables the rare coexistence of robust topological edge states and frustration-induced dense modes within a single passive lattice (Fig. 5a, b). The two phenomena occupy distinct spectral regions within the same projected Hamiltonian H_a. Topological edge modes are localized within the dimerization-induced bandgap, governed by $|k_{\mathrm{inter}} - k_{\mathrm{intra}}|$, while frustrated modes accumulate near the band edge, driven by the sign conflict $k_{\mathrm{LR}} < 0$. At $\theta_c = 70°$, a topological bandgap opens, hosting localized edge modes ($n = 10, 11$) that overlap with the frustrated regime ($n = 1 - 9$). Because moderate long-range coupling shifts band-edge modes without closing the topological gap,

ARTICLE IN PRESS

the two phenomena are spectrally robust against each other. Experimental measurements (Fig. 5c-e) show strong energy confinement at the boundary ($m = 1$), with row polarization (P) peaking within the bandgap, while the frustrated bulk modes remain spectrally distinct and independently addressable. The corresponding experimental dynamics corresponding to the topological phases are shown in Supplementary Videos 3, 4.

Broader implications and related platforms

Our anisotropy-driven projection goes beyond basis transformation, enabling a physical reduction of the Hilbert space into spectrally separated Hamiltonians. This framework provides a macroscopic analogue to quantum Hamiltonian engineering. Specifically, our system mimics the phonon-mediated interactions of trapped-ion platforms and parallels the geometric programming of frustrated states in Rydberg atom arrays. By establishing this classical–quantum correspondence, our work offers a unified perspective for exploring complex physical regimes across programmable metamaterials and engineered spin models.

Beyond classical metamaterials, interaction sign control is a key ingredient in quantum simulation platforms [34, 35], where interactions are often mediated by collective phononic modes. While the present approach based on rotation-controlled anisotropy is not directly transferable to such quantum many-body systems, it establishes a passive and static route for shaping effective interactions at the phonon-mediated level. In this sense, our results offer a classical framework that may provide insight into alternative strategies for interaction engineering beyond conventional active control schemes. This perspective opens opportunities for programmable wave systems, analog simulation [36], and the exploration of engineered excitation landscapes across both classical and quantum platforms.

The coupling-sign engineering demonstrated here extends naturally to other platforms where central-force interactions combine with local anisotropic confinement. Dusty plasma crystals on two-dimensional substrates [37, 38] are a compelling example, where Yukawa-type inter-particle forces provide central-force coupling, and substrate-induced anisotropy could program the sign-conflict configurations explored here, with phonon spectra directly accessible through laser-scattering diagnostics. Colloidal ice systems [39], where time-dependent external fields modulate particle interactions on periodic substrates, represent another candidate for engineering dynamical frustration. While typically overdamped, the sign-conflict condition $\Phi < 0$ is a geometric constraint on coupling loops that does not require underdamped dynamics. Active fluids in patterned networks [40] may exhibit related self-organized frustrated flow patterns, connecting our classical framework to non-equilibrium systems. On the quantum side, qubit spin ice platforms [41] offer an avenue for exploring quantum analogues of the frustrated and topological states demonstrated here, given their programmable effective spin–spin interactions and the central role of competing interactions in their design.

ARTICLE IN PRESS

ARTICLE IN PRESS

Conclusions.

We have demonstrated that local anisotropy provides a Hamiltonian-level control parameter for controlling wave phenomena in lattice systems. By rotating anisotropic confinement, the effective interaction in projected local degrees of freedom can be continuously tuned, enabling sign-reversible couplings within a fixed lattice. This mechanism generates competing interactions that produce wave frustration while simultaneously driving topological band inversion, allowing frustration and topology to coexist in a single passive lattice. Furthermore, the strong anisotropy enables the projection of spectrally separated manifolds, each accessing disparate coupling regimes, ranging from nonlocal horizontal interactions to dimerized topological phases, due to the 90° shift in effective coupling across manifolds (Supplementary Note 4, Fig. S4; Supplementary Note 5, Fig. S5; Supplementary Video 5). This multi-manifold behavior provides a versatile platform for frequency-dependent control, where different wave physics can be programmed and manipulated independently within a unified lattice structure.

Importantly, such sign-reversible effective couplings arise generically from central-force power-law interactions of the form $F(d) = Ad^p$, which, under prestress, produce longitudinal and transverse stiffness components of opposite sign. These central-force interactions are ubiquitous across elastic, electrostatic, and phonon-mediated systems, where the effective exponent p can be engineered through geometry or confinement. While our physical implementation realizes this mechanism through the geometric tilting of anisotropic cantilevers in an elastic lattice, the requisite trapping potentials can be established through a variety of non-contact fields such as optical, electrostatic, or electromagnetic fields. Although such non-contact fields are not applied to the current elastic system, the ubiquity of these central-force interactions across scales suggests that our findings offer a general strategy for programming synthetic Hamiltonians in platforms ranging from phonon-mediated systems to cold-atom arrays.

Looking ahead, several natural extensions of this work are of interest. Introducing local defects, such as a change in anisotropy angle at one or a few sites, would create a tunable potential landscape for topologically protected modes, analogous to domain walls in Su-Schrieffer-Heeger chains, enabling spatially addressable localized resonances without modifying the bulk lattice structure. Exploring alternative lattice geometries, including honeycomb, kagome, or Lieb configurations within the same central-force framework, would provide access to richer topological invariants, multi-band frustration, and potentially flat bands with sign-controlled coupling. The inherent 90° orthogonality between a- and b-manifold effective couplings further suggests that alternative lattice angles and bond configurations can be used to rationally design manifold-specific coupling architectures for multi-channel, frequency-selective wave control.

ARTICLE IN PRESS

ARTICLE IN PRESS

Methods

Device and Experimental Setup

The movable magnets ($A = 2 \times 10^{-9} N/m^p$ and $p \approx -4.1$) are attached to thin, vertical acrylic cantilevers (Elastic modulus $E = 3$ GPa) with rectangular cross section ($a_0 = 1.0$ mm and $b_0 = 3.5$ mm) and $l_c = 63$ mm length (Plastruct). The bending stiffnesses are characterized by $k_a = \frac{E a_0^3 b_0}{4 l_c^3}$ and $k_b = \frac{E b_0^3 a_0}{4 l_c^3}$. The bases of the cantilevers are firmly fixed to a 3D printed plate attached to an optical breadboard. Fixed magnets are placed around the movable magnets and are held by a 3D-printed plate, 10 mm thick (Markforged Mark Two, Markforged Inc.). The disc magnets (both movable and fixed) are neodymium rare earth permanent magnets of N42 grade (Element Magnets Inc., 6.35 mm in diameter and 3.175 mm thick). The experimental setup is shown in Supplementary Note 6, Fig. S6. The top surfaces of the movable magnets have tracking markers (a black circular line with white core). For observation of dispersion relations, one magnet ($m = 1$) is excited using a mechanical shaker with built-in amplifiers (K2003E01, The Modal Shop) over an excitation frequency range of 20-50 Hz, with a 1 Hz interval. The motion of the magnets is captured under flicker-free light illumination (Nila Varsa, Tech Imaging Services, Inc.) using a high-speed camera (BFS-U3-04S2C-CS, Flir) operating at a frame rate of 200 fps with an exposure time of 100 μs. The mechanical shaker and high-speed camera are synchronized by a data acquisition chassis equipped with an output module (50 kS/s, National Instruments). The captured images are processed to extract displacements, using digital image correlation and point tracking algorithms with GOM Correlate 2020, a commercial software.

Jacobian-based derivation of the central-force stiffnesses, $k_\perp$ and $k_\parallel$

We consider a central force of the form $\mathbf{F}(\mathbf{r}) = F(d) \begin{pmatrix} \cos\theta_b \\ \sin\theta_b \end{pmatrix}$, with a distance-dependent magnitude $F(d)$ and the distance $d = \sqrt{x^2 + y^2}$. The force is along the bond direction (the unit vector $\hat{\mathbf{n}} = (\cos\theta_b, \sin\theta_b)$).

The Jacobian of the force is $\mathbf{J} = \frac{\partial \mathbf{F}}{\partial(x,y)}$, and the linearized stiffness matrix at $d = d_0$ is defined as $\mathbf{M} = -\mathbf{J}$. The Jacobian components can be evaluated explicitly, leading to the stiffness matrix:

$$\mathbf{M}(\theta_b) = -F'(d_0) \begin{pmatrix} \cos^2\theta_b & \cos\theta_b \sin\theta_b \\ \cos\theta_b \sin\theta_b & \sin^2\theta_b \end{pmatrix} - \frac{F(d_0)}{d_0} \begin{pmatrix} \sin^2\theta_b & \cos\theta_b \sin\theta_b \\ \cos\theta_b \sin\theta_b & \cos^2\theta_b \end{pmatrix}. \tag{5}$$

This is equivalent to $\mathbf{M}(\theta_b) = -F'(d_0)\hat{\mathbf{n}}\hat{\mathbf{n}}^T - \frac{F(d_0)}{d_0}(\mathbf{I} - \hat{\mathbf{n}}\hat{\mathbf{n}}^T)$. Since $\hat{\mathbf{n}}\hat{\mathbf{n}}^T$ and $\mathbf{I} - \hat{\mathbf{n}}\hat{\mathbf{n}}^T$ correspond to projectors parallel ($\mathbf{P}_{ij}^{\parallel}$) and perpendicular ($\mathbf{P}_{ij}^{\perp}$) to the bond, respectively, we define the parallel and transverse stiffnesses as

$$k_\parallel = -F'(d_0), \qquad k_\perp = -\frac{F(d_0)}{d_0}, \tag{6}$$

leading to $\mathbf{M}(\theta_b) = k_\parallel \mathbf{P}_{ij}^{\parallel} + k_\perp \mathbf{P}_{ij}^{\perp}$ (same as Eq. 2).

The resulting stiffness matrix takes the form

$$\mathbf{M}(\theta_b) = \begin{bmatrix} k_\parallel \cos^2\theta_b + k_\perp \sin^2\theta_b & (k_\parallel - k_\perp)\cos\theta_b \sin\theta_b \\ (k_\parallel - k_\perp)\cos\theta_b \sin\theta_b & k_\parallel \sin^2\theta_b + k_\perp \cos^2\theta_b \end{bmatrix}. \tag{7}$$

To obtain the effective coupling stiffness along an arbitrary direction $\hat{\mathbf{e}} = (\cos\theta_c, \sin\theta_c)$, we consider a displacement $\delta\mathbf{r} = s\,\hat{\mathbf{e}}$. The effective stiffness is then defined as $k_{\text{eff}} = \hat{\mathbf{e}}^{\mathsf{T}} \mathbf{M}(\theta_b) \hat{\mathbf{e}}$.

ARTICLE IN PRESS

A straightforward calculation yields

$$\begin{aligned} k_{\text{eff}}(\theta_b, \theta_c) &= k_{\parallel} \cos^2(\theta_b - \theta_c) + k_{\perp} \sin^2(\theta_b - \theta_c), \\ &= k_{\perp} + (k_{\parallel} - k_{\perp}) \cos^2(\theta_b - \theta_c). \end{aligned} \tag{8}$$

For a repulsive central force $F(d_0) > 0$, the transverse stiffness satisfies $k_{\perp} < 0$, allowing the effective stiffness to change sign purely through geometric projection.

Decomposed Hamiltonians H_a and H_b, and XY-like phase model

When the local confinement is diagonal in the $\{a, b\}$ basis and the anisotropy is sufficiently strong $k_a \ll k_b$ or $k_a \gg k_b$, Projection of the 2D Hamiltonian onto the two orthogonal anisotropy directions leads to its decomposition:

$$H = H_a \oplus H_b. \tag{9}$$

The symbol $\oplus$ denotes a direct sum, implying that the two 1D Hamiltonians (H_a and H_b) act on orthogonal modal subspaces and remain completely decoupled ($H_{ab} = 0$). The Hamiltonian projected onto the soft axis $\vec{\mathbf{a}}$ is

$$H_a = \sum_i \left(\frac{1}{2} m \dot{a}_i^2 + \frac{1}{2} k_a a_i^2 \right) + \frac{1}{2} \sum_{\langle i,j \rangle} k_{\text{eff}}^{(ij)} \left(a_i - a_j \right)^2, \tag{10}$$

where $k_{\text{eff}}^{(ij)}(\alpha)$ is the effective coupling stiffness obtained from the geometric projection of the physical interaction onto the local a axis.

Similarly, the Hamiltonian projected onto the stiff axis b is

$$H_b = \sum_i \left(\frac{1}{2} m \dot{b}_i^2 + \frac{1}{2} k_b b_i^2 \right) + \frac{1}{2} \sum_{\langle i,j \rangle} k_{\text{eff},b}^{(ij)} \left(b_i - b_j \right)^2. \tag{11}$$

Here $k_{\text{eff},b}^{(ij)}(\beta) = k_{\text{eff}}^{(ij)}(\alpha + 90^\circ)$ with β being the angle between the bond direction and the local b axis.

The phase relation between the sites can be described by XY-like model, as the correlation Hamiltonian $H_{ij} = -k_{\mathbf{eff}} a_i a_j$ is obtained from Eq. 10 and Eq. 11. With $a_i(t) = A_i \cos(\omega t + \phi_i)$, the time-averaged correlation Hamiltonian is given by

$$\langle H_{ij}^{\text{corr}} \rangle = -A_i A_j k_{\mathbf{eff}} \cos(\phi_i - \phi_j) \tag{12}$$

Equation 12 is modified to include phase accumulation corresponding to qd, resulting in

$$\langle H_{ij}^{\text{corr}} \rangle = -A_i A_j k_{\mathbf{eff}} \cos(\phi_i - \phi_j - qd) \tag{13}$$

Eigenvalue Analysis of 1D and 2D models

With cantilever-induced local anisotropy, the 2D (lossless) linear model of the unit cell consisting of masses A and B is given by

$$(\mathbf{K}_{2D}(\theta_c) - m\omega^2 \mathbf{I}) \begin{bmatrix} u_A \\ v_A \\ u_B \\ v_B \end{bmatrix} = 0, \tag{14}$$

ARTICLE IN PRESS

with displacements u and v along x and y, respectively, and the Bloch stiffness matrix for constant local stiffness ($\mathbf{K}_i(\theta_c) = \mathbf{K}(\theta_c)$ for all sites tilted by the same angle) is represented as

$$\mathbf{K}_{2D}(\theta_c) = \begin{bmatrix} \mathbf{M}_t + \mathbf{K}(\theta_c) & -\mathbf{M}_{\text{intra}} - \mathbf{M}_{\text{inter}} e^{-iqd_0} \\ -\mathbf{M}_{\text{intra}} - \mathbf{M}_{\text{inter}} e^{+iqd_0} & \mathbf{M}_t + \mathbf{K}(\theta_c) \end{bmatrix}. \tag{15}$$

with $\mathbf{M}_t = \mathbf{M}_{\text{intra}} + \mathbf{M}_{\text{inter}} + \mathbf{M}_{\text{fix}} + 2\mathbf{M}_{\text{LR}}\left[1 - \cos(qd_0)\right]$ and $\mathbf{M}_{\text{fix}} = \mathbf{M}_{\text{intra}} + \mathbf{M}_{\text{inter}}$ (coupling from the fixed magnets). Here, from Eq. 7, $\mathbf{M}_{\text{intra}}$, $\mathbf{M}_{\text{inter}}$, and $\mathbf{M}_{\text{LR}}$ are obtained from the Jacobian matrix $\mathbf{M}(\theta_b)$, depending on the bond direction θ_b: $\theta_b = -\theta$ for $\mathbf{M}_{\text{intra}}$, $\theta_b = \theta$ for $\mathbf{M}_{\text{inter}}$, and $\theta_b = 0°$ for $\mathbf{M}_{\text{LR}}$.

For $k_a \ll k_b$ and thereby two decoupled 1D Hamiltonians H_a and H_b, the 1D equivalent (lossless) linear model (a-manifold) is given by

$$(\mathbf{K}_{1D}^{(a)} - m\omega^2 \mathbf{I}) \begin{bmatrix} a_A \\ a_B \end{bmatrix} = 0, \tag{16}$$

Here the Bloch stiffness matrix is given by

$$\mathbf{K}_{1D}^{(a)}(q) = \begin{bmatrix} k_t + k_a & -k_{\text{intra}} - k_{\text{inter}}\, e^{-iqd_0} \\ -k_{\text{intra}} - k_{\text{inter}}\, e^{+iqd_0} & k_t + k_a \end{bmatrix}, \tag{17}$$

with $k_t = k_{\text{intra}} + k_{\text{inter}} + k_{\text{fix}} + 2k_{\text{LR}}\left[1 - \cos(qd_0)\right]$ and $k_{\text{fix}} = k_{\text{intra}} + k_{\text{inter}}$. Considering bonds $\mathbf{d}_{\text{inter}} = (\cos\theta, \sin\theta)$, $\mathbf{d}_{\text{intra}} = (\cos\theta, -\sin\theta)$ at $\theta = \pi/3$, and $\mathbf{d}_{\text{LR}} = (1, 0)$, from Eq. 3 the effective coupling for $k_\perp = -A\, d_0^{(p-1)} = -k_0$ and $k_\parallel = -A\, p\, d_0^{(p-1)}$ is given by

$$k_{\text{eff}}^{(ij)} = \begin{cases} k_{\text{intra}} = -\left[(p-1)\cos^2(\theta + \theta_c) + 1\right] k_0 \\ k_{\text{inter}} = -\left[(p-1)\cos^2(\theta - \theta_c) + 1\right] k_0 \\ k_{\text{LR}} = -\left[(p-1)\cos^2(\theta_c) + 1\right] k_0 \end{cases} \tag{18}$$

Other formulas

Modal polarization ratio (along the local a-axis), P_a

P_a is the fraction of the eigenvector energy projected onto the local a-axis (summed over both sites A and B within the unit cell), i.e.

$$P_a = \frac{E_a}{E_a + E_b}, \tag{19}$$

where $E_a = \sum_{s=A,B} \left|\mathbf{u}_s \cdot \vec{\mathbf{a}}\right|^2, \qquad E_b = \sum_{s=A,B} \left|\mathbf{u}_s \cdot \vec{\mathbf{b}}\right|^2.$

Here $\mathbf{u}_s = (u_s, v_s)^\top$ denotes the displacement at site s, and the local orthonormal basis vectors are defined as $\vec{\mathbf{a}} = (\cos\theta_c, \sin\theta_c)^\top, \qquad \vec{\mathbf{b}} = (-\sin\theta_c, \cos\theta_c)^\top$.

Row-polarization, $P(f)$

We define the frequency-dependent polarization as

$$P(f) = \frac{E_{\text{top}}(f) - E_{\text{bot}}(f)}{E_{\text{top}}(f) + E_{\text{bot}}(f)}, \tag{20}$$

ARTICLE IN PRESS

where the energy on the top and bottom rows is given by $E_{\text{top/bot}}(f) = \sum_m \left|u_{\text{top/bot}}(m))\right|^2$.

The polarization satisfies:

$$\begin{cases} \mathrm{P} = 0 & \text{equal energy on the top and bottom rows,} \\ \mathrm{P} = +1 & \text{only the top row responds,} \\ \mathrm{P} = \text{-}1 & \text{only the bottom row responds.} \end{cases}$$

Mode participation, S_n

Measured complex displacement field (at one drive frequency) $U(f)$ can be modeled as a linear combination of eigenmodes :

$$\mathbf{U}(f) \approx \sum_{n}^{N} S_n(f) a_n \tag{21}$$

with $S_n(f)$ being the modal contribution and a_n being the n-th mode shape (from eigenvalue analysis). The modal contribution is calculated by $S_n = (\mathbf{a}^T\mathbf{a})^{-1}\mathbf{a}^T\mathbf{U}$ with $\mathbf{a} = [a_{n=1}, ..., a_{n=N}]$.

Data availability

The numerical data underlying the figures in this study, including dispersion relations, mode profiles, eigenfrequency spectra, and phase measurements, are provided as Supplementary Data files accompanying this article. The source data for Figs. 1–5 are in Supplementary Data 1. Additional data supporting the findings of this study are available from the corresponding author upon request.

Funding

This research received no external funding.

References

[1] Ling Lu, John D Joannopoulos, and Marin Soljačić. Topological photonics. *Nature photonics*, 8(11):821–829, 2014.

[2] Guancong Ma, Meng Xiao, and Che Ting Chan. Topological phases in acoustic and mechanical systems. *Nature Reviews Physics*, 1(4):281–294, 2019.

[3] RF Wang, Cristiano Nisoli, Rafael Sá de Freitas, J Li, W McConville, BJ Cooley, MS Lund, N Samarth, C Leighton, VH Crespi, et al. Artificial 'spin ice'in a geometrically frustrated lattice of nanoscale ferromagnetic islands. *Nature*, 439(7074):303–306, 2006.

[4] Leon Balents. Spin liquids in frustrated magnets. *nature*, 464(7286):199–208, 2010.

[5] Younes Ra'di, Dimitrios L Sounas, and Andrea Alù. Metagratings: Beyond the limits of graded metasurfaces for wave front control. *Physical review letters*, 119(6):067404, 2017.

ARTICLE IN PRESS

ARTICLE IN PRESS

[6] Lauriane Chomaz, Rick MW van Bijnen, Daniel Petter, Giulia Faraoni, Simon Baier, Jan Hendrik Becher, Manfred J Mark, Falk Waechtler, Luis Santos, and Francesca Ferlaino. Observation of roton mode population in a dipolar quantum gas. *Nature physics*, 14(5):442–446, 2018.

[7] Yi Chen, Muamer Kadic, and Martin Wegener. Roton-like acoustical dispersion relations in 3d metamaterials. *Nature communications*, 12(1):3278, 2021.

[8] B Andrei Bernevig, Taylor L Hughes, and Shou-Cheng Zhang. Quantum spin hall effect and topological phase transition in hgte quantum wells. *science*, 314(5806):1757–1761, 2006.

[9] Charles L Kane and Tom C Lubensky. Topological boundary modes in isostatic lattices. *Nature Physics*, 10(1):39–45, 2014.

[10] Marc Serra-Garcia, Valerio Peri, Roman Süsstrunk, Osama R Bilal, Tom Larsen, Luis Guillermo Villanueva, and Sebastian D Huber. Observation of a phononic quadrupole topological insulator. *Nature*, 555(7696):342–345, 2018.

[11] Robert Keil, Charles Poli, Matthias Heinrich, Jake Arkinstall, Gregor Weihs, Henning Schomerus, and Alexander Szameit. Universal sign control of coupling in tight-binding lattices. *Physical review letters*, 116(21):213901, 2016.

[12] Chiara Bigi, Matteo Dürrnagel, Lennart Klebl, Armando Consiglio, Ganesh Pokharel, Marta Zonno, François Bertran, Patrick Le Fèvre, Thomas Jaouen, Hulerich C Tchouekem, et al. Pomeranchuk instability from electronic correlations in CsTi3Bi5 kagome metal. *Nature Communications*, 17:325, 2025.

[13] Simon J Evered, Marcin Kalinowski, Alexandra A Geim, Tom Manovitz, Dolev Bluvstein, Sophie H Li, Nishad Maskara, Hengyun Zhou, Sepehr Ebadi, Muqing Xu, et al. Probing the kitaev honeycomb model on a neutral-atom quantum computer. *Nature*, 645(8080):341–347, 2025.

[14] Kihwan Kim, M-S Chang, Simcha Korenblit, Rajibul Islam, Emily E Edwards, James K Freericks, G-D Lin, L-M Duan, and Christopher Monroe. Quantum simulation of frustrated ising spins with trapped ions. *Nature*, 465(7298):590–593, 2010.

[15] Rainer Blatt and Christian F Roos. Quantum simulations with trapped ions. *Nature Physics*, 8(4):277–284, 2012.

[16] Antoine Browaeys and Thierry Lahaye. Many-body physics with individually controlled Rydberg atoms. *Nature Physics*, 16(2):132–142, 2020.

[17] Giulia Semeghini, Harry Levine, Alexander Keesling, Sepehr Ebadi, Tout T Wang, Dolev Bluvstein, Ruben Verresen, Hannes Pichler, Marcin Kalinowski, Rhine Samajdar, et al. Probing

ARTICLE IN PRESS

ARTICLE IN PRESS

topological spin liquids on a programmable quantum simulator. *Science*, 374(6572):1242–1247, 2021.

[18] Lea Sirota, Roni Ilan, Yair Shokef, and Yoav Lahini. Non-Newtonian topological mechanical metamaterials using feedback control. *Physical Review Letters*, 125(25):256802, 2020.

[19] Lianchao Wang, Julio A Iglesias Martínez, Gwenn Ulliac, Bing Wang, Vincent Laude, and Muamer Kadic. Non-reciprocal and non-Newtonian mechanical metamaterials. *Nature Communications*, 14(1):4778, 2023.

[20] Dimitrios L Sounas and Andrea Alù. Non-reciprocal photonics based on time modulation. *Nature Photonics*, 11(12):774–783, 2017.

[21] Alexander Impertro, SeungJung Huh, Simon Karch, Julian F Wienand, Immanuel Bloch, and Monika Aidelsburger. Strongly interacting meissner phases in large bosonic flux ladders. *Nature Physics*, 21(6):895–901, 2025.

[22] Anne S Meeussen, Erdal C Oğuz, Yair Shokef, and Martin van Hecke. Topological defects produce exotic mechanics in complex metamaterials. *Nature Physics*, 16(3):307–311, 2020.

[23] Jayson Paulose, Bryan Gin-ge Chen, and Vincenzo Vitelli. Topological modes bound to dislocations in mechanical metamaterials. *Nature Physics*, 11(2):153–156, 2015.

[24] Feng Gao, Xiao Xiang, Yu-Gui Peng, Xiang Ni, Qi-Li Sun, Simon Yves, Xue-Feng Zhu, and Andrea Alù. Orbital topological edge states and phase transitions in one-dimensional acoustic resonator chains. *Nature Communications*, 14(1):8162, 2023.

[25] Max Born and Kun Huang. *Dynamical theory of crystal lattices*. Oxford university press, 1996.

[26] Sergey Bravyi, David P DiVincenzo, and Daniel Loss. Schrieffer–wolff transformation for quantum many-body systems. *Annals of physics*, 326(10):2793–2826, 2011.

[27] Jayson Paulose, Anne S Meeussen, and Vincenzo Vitelli. Selective buckling via states of self-stress in topological metamaterials. *Proceedings of the National Academy of Sciences*, 112(25):7639–7644, 2015.

[28] Yuanyuan Zong, Shiqiang Xia, Liqin Tang, Daohong Song, Yi Hu, Yumiao Pei, Jing Su, Yigang Li, and Zhigang Chen. Observation of localized flat-band states in kagome photonic lattices. *Optics Express*, 24(8):8877–8885, 2016.

[29] Han-Rong Xia, Ziyao Wang, Yunrui Wang, Zhen Gao, and Meng Xiao. Fully flat bands in a photonic dipolar kagome lattice. *Physical Review Letters*, 135(17):176902, 2025.

[30] Elliott Lieb, Theodore Schultz, and Daniel Mattis. Two soluble models of an antiferromagnetic chain. *Annals of Physics*, 16(3):407–466, 1961.

ARTICLE IN PRESS

ARTICLE IN PRESS

[31] Taehwa Lee, Bertin Many Manda, Xiaopeng Li, Ziqi Yu, Georgios Theocharis, and Chiara Daraio. Control of multimodal topological edge modes in magnetoelastic lattices. *Physical Review Applied*, 21(2):024049, 2024.

[32] Taehwa Lee, Xiaopeng Li, Ziqi Yu, Hyung-Suk Kwon, and Chiara Daraio. Mechanical spin waves in a nonlocal discrete magnetoelastic lattice with negative group velocity. *Advanced Physics Research*, 4:2400197, 2025.

[33] Soobin Park, Minjae Huh, Chris Jozwiak, Eli Rotenberg, Aaron Bostwick, and Keun Su Kim. Electronic rotons and wigner crystallites in a two-dimensional dipole liquid. *Nature*, 634(8035): 813–817, 2024.

[34] Kevin A Gilmore, Matthew Affolter, Robert J Lewis-Swan, Diego Barberena, Elena Jordan, Ana Maria Rey, and John J Bollinger. Quantum-enhanced sensing of displacements and electric fields with two-dimensional trapped-ion crystals. *Science*, 373(6555):673–678, 2021.

[35] Pimonpan Sompet, Sarah Hirthe, Dominik Bourgund, Thomas Chalopin, Julian Bibo, Joannis Koepsell, Petar Bojović, Ruben Verresen, Frank Pollmann, Guillaume Salomon, et al. Realizing the symmetry-protected haldane phase in fermi–hubbard ladders. *Nature*, 606(7914):484–488, 2022.

[36] Dhireesha Kudithipudi, Catherine Schuman, Craig M Vineyard, Tej Pandit, Cory Merkel, Rajkumar Kubendran, James B Aimone, Garrick Orchard, Christian Mayr, Ryad Benosman, et al. Neuromorphic computing at scale. *Nature*, 637(8047):801–812, 2025.

[37] J Beckers et al. Physics and applications of dusty plasmas: The perspectives 2023. *Physics of Plasmas*, 30:120601, 2023.

[38] Y Huang, W Li, C Reichhardt, C J O Reichhardt, and Yan Feng. Phonon spectra of a two-dimensional solid dusty plasma modified by two-dimensional periodic substrates. *Physical Review E*, 105(1):015202, 2022.

[39] Antonio Ortiz-Ambriz, Cristiano Nisoli, Charles Reichhardt, Cynthia J O Reichhardt, and Pietro Tierno. Colloquium: Ice rule and emergent frustration in particle ice and beyond. *Reviews of Modern Physics*, 91(4):041003, 2019.

[40] Mathieu Le Verge-Serandour and Karen Alim. Active fluids navigate networks by solving sudoku-like problems. *Nature*, 627:39–40, 2024.

[41] Andrew D King, Cristiano Nisoli, Edward D Dahl, Gabriel Poulin-Lamarre, and Alejandro Lopez-Bezanilla. Qubit spin ice. *Science*, 373(6554):576–580, 2021.

ARTICLE IN PRESS

ARTICLE IN PRESS

Author contributions

T.L. conceived the idea, led the research, performed experiments, and wrote the manuscript. Z.Y. contributed to writing and data interpretation. X.S. and H.-S.K. contributed to data interpretation and manuscript review. C.D. contributed to manuscript review, discussion, and data interpretation.

Competing interests

T.L. is a named inventor on patent applications related to the methods described in this work. All other authors declare no competing interests.

ARTICLE IN PRESS

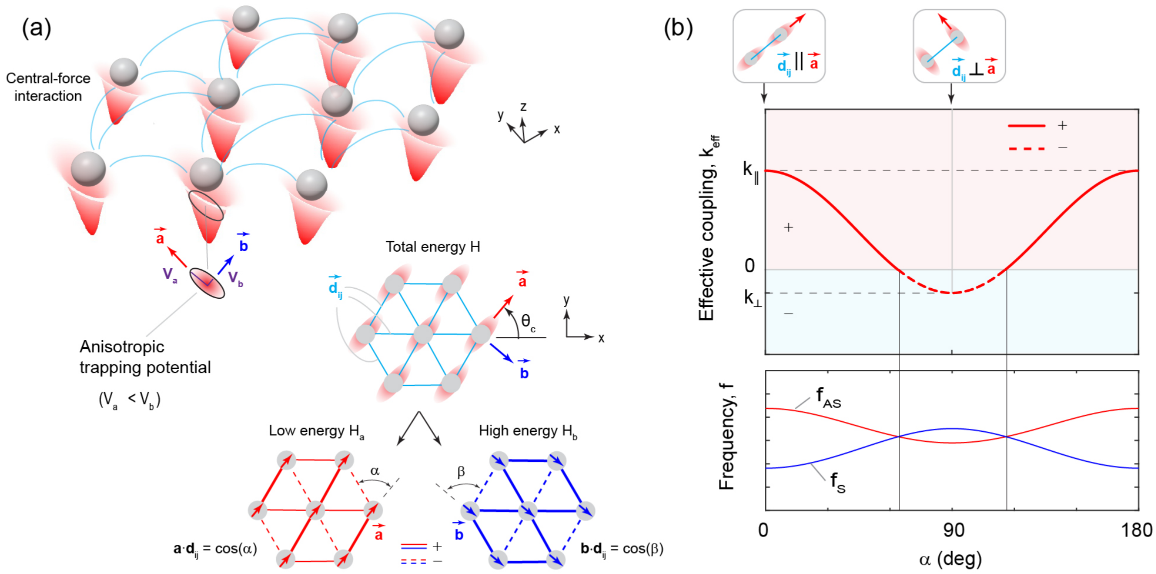

Figure 1. Local anisotropy-controlled interaction sign and strength (a) Schematic of the central-force elastic lattice with anisotropic trapping. Each site is defined by an anisotropic potential well ($V_a < V_b$) with local principal axes $\vec{\mathbf{a}}$ and $\vec{\mathbf{b}}$ (red and blue arrows). Neighboring sites are coupled via generalized central forces (blue dashed lines) characterized by longitudinal and transverse stiffness ($k_\parallel, k_\perp$). The total Hamiltonian H is decomposed into low-energy (H_a) and high-energy (H_b) components. The projection angles (α, β) between the principal axes and the bond vectors ($\mathbf{d}_{ij}$) dictate the interaction sign, where solid red lines denote positive coupling (+) and dashed lines indicate negative coupling (−). (b) Effective coupling k_{eff} as a function of the projection angle (α). The coupling varies continuously from positive (solid red line) to negative (dashed red line) values, with limits set by $k_\parallel$ ($\alpha = 0°$) and $k_\perp$ ($\alpha = 90°$). The lower panel shows the resulting mode reordering in a two-mass system, where negative coupling manifests as the antisymmetric mode frequency (f_{AS}) below the symmetric mode frequency (f_{S}).

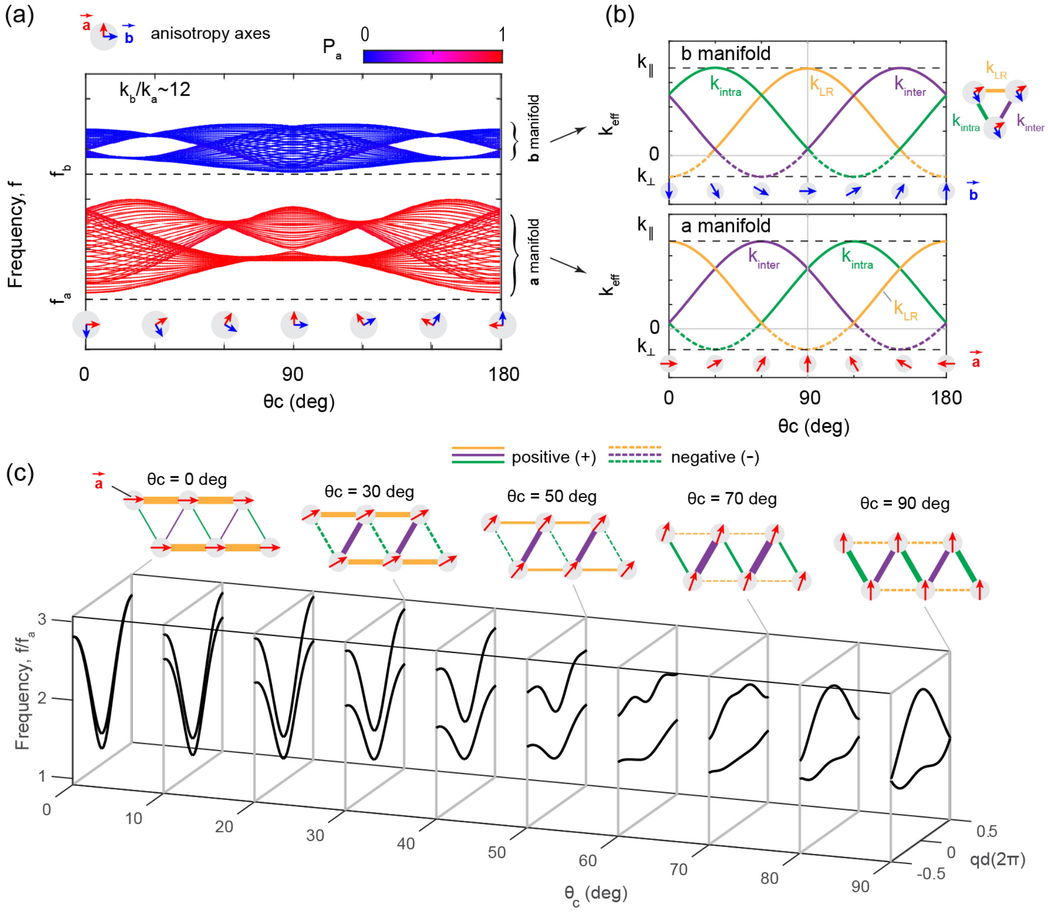

Figure 2. Spectral separation and programmable lattice dynamics. (a) Dispersion spectrum of an infinite periodic zigzag lattice as a function of the anisotropy angle θ_c. Strong local anisotropy ($k_b/k_a \approx 12$) induces a wide spectral gap between the low-frequency a-manifold and high-frequency b-manifold. The color scale indicates the projection parameter P_a, where $P_a = 1$ (red) and $P_a = 0$ (blue) denote pure a- and b-manifold modes, respectively, confirming robust manifold isolation and negligible cross-coupling. (b) Evolution of nearest-neighbor (intra and inter) and long-range (LR) effective couplings k_{eff} for both manifolds. Continuous rotation of θ_c enables control over the magnitude and sign (solid for positive, dashed for negative) of each interaction type. The effective coupling of the a-manifold is shifted by 90° relative to the b-manifold. (c) Representative lattice configurations for selected angles θ_c. Evolution of the a-manifold dispersion for anisotropy angles (every 10°), illustrating systematic evolution of coupling regimes with anisotropy rotation.

ARTICLE IN PRESS

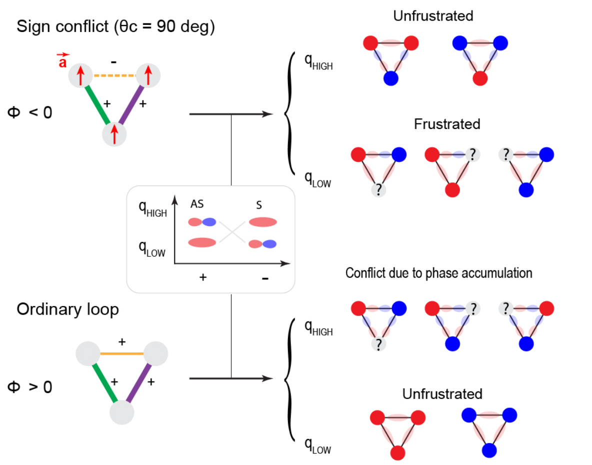

Figure 3. Frequency-selective frustration. A triangular loop with a negative interaction product, $\Phi = \mathrm{sign}(+,+,-) < 0$, exhibits frustration at small wavenumber (q_{LOW}), corresponding to long-wavelength modes. In contrast, an ordinary loop with $\Phi = \mathrm{sign}(+,+,+) > 0$ develops phase conflict at large wavenumber (q_{HIGH}), arising from phase accumulation along the loop.

ARTICLE IN PRESS

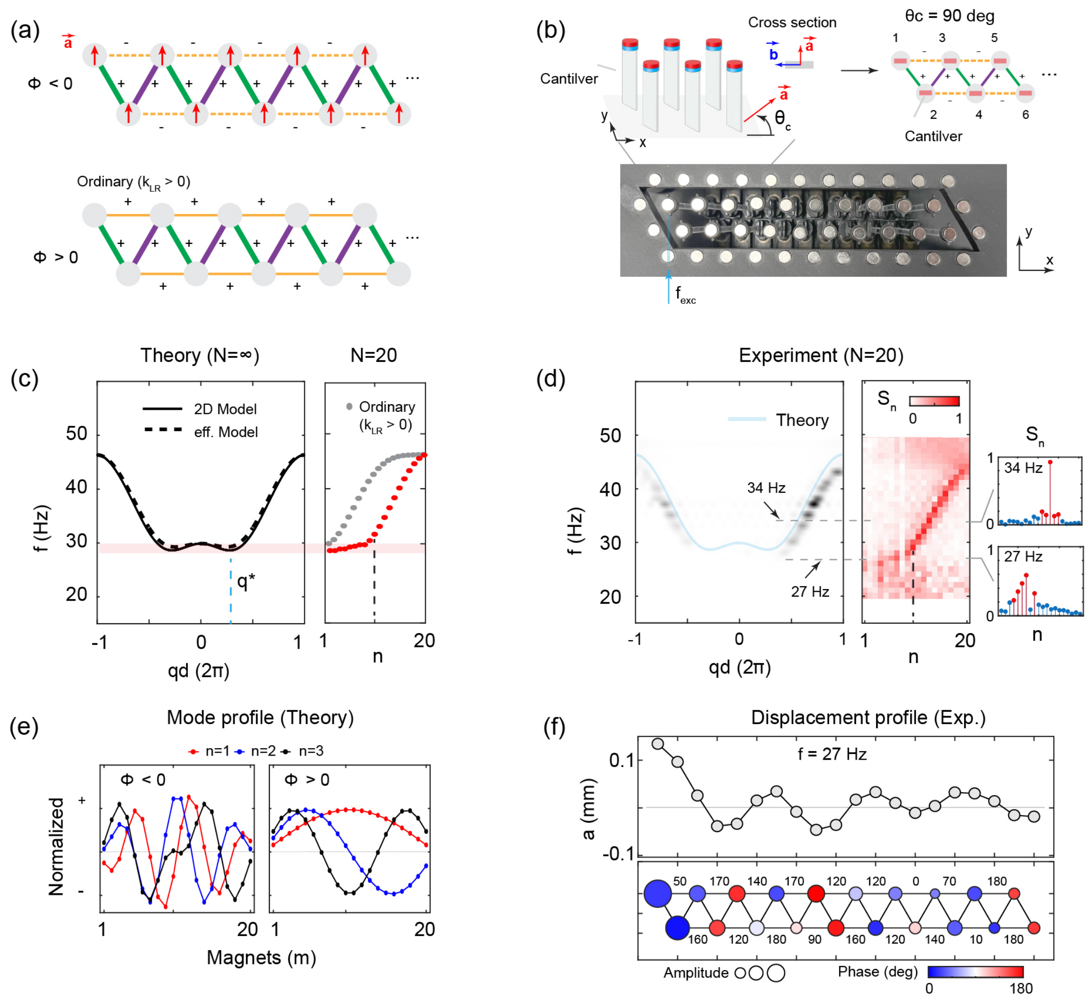

Figure 4. Wave frustration induced by sign-controlled long-range coupling. (a) Schematic of the zigzag lattice in the frustration regime ($\theta_c = 90°$, a-manifold), for $\Phi < 0$. Dashed lines denote negative effective coupling. Ordinary lattice with ($k_{\mathrm{LR}} > 0$) for $\Phi > 0$. (b) Experimental realization of the frustration lattice. An illustration and photograph of the magnet array with equal spacing are shown. Local anisotropy is introduced using rectangular cantilevers. The soft axis $\vec{\mathbf{a}}$ (normal to the wider face of the cross-section) is aligned to achieve projection-controlled coupling. (c) Theoretical dispersion of the infinite lattice obtained from the 2D model (solid line), compared with that obtained from the effective couplings (dashed). In the right panel, discrete eigenfrequencies of the finite lattice ($N = 20$) are plotted with those of the ordinary lattice ($k_{\mathrm{LR}} > 0$) for comparison. (d) Experimentally characterized dispersion and corresponding modal contribution S_n (2D surface plot over discrete frequency and mode index). Representative S_n at 27 Hz highlights mode crowding in the frustration regime, while S_n at 34 Hz demonstrates effective single mode excitation. (e) Theoretical mode profiles of the finite lattice ($N = 20$) for the first three modes ($n = 1, 2, 3$): frustration lattice (left) versus ordinary lattice (right). (f) (top) Measured displacement profile at 27 Hz and (bottom) corresponding amplitude-phase diagram with the amplitude (circle size) and phase (color). Bonds along the top and bottom rows exhibit finite phase differences between connected masses.

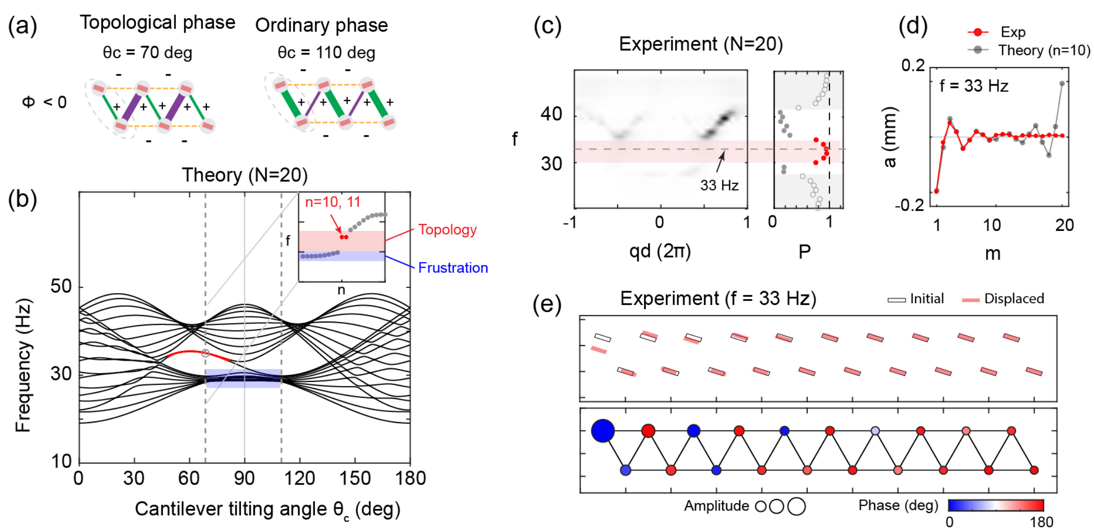

Figure 5. Coexistence of topology and frustration. (a) Schematic of zigzag lattices for the topological phase ($\theta_c = 70°$) and the ordinary phase ($\theta_c = 110°$). (b) Eigenfrequencies of the finite lattice ($N = 20$, a-manifold) as a function of θ_c, showing the emergence of a topological bandgap and edge modes. The inset (at $\theta_c = 70°$) highlights edge modes ($n = 10, 11$) and mode crowding (blue shading), demonstrating coexistence of frustration and topology. (c) Experimentally characterized dispersion relation with the bandgap highlighted (red shading). The right panel shows polarity P ($P = 1$ top-row dominant, $P = 0$ bottom-row dominant). The topological mode exhibits $P = 1$ due to dominant displacement of odd magnets (excitation at $m = 1$). (d) Measured displacement profile at 33 Hz (red) compared with the theoretical mode profile ($n = 10$, antisymmetric edge mode). (e) Measured displacement profiles shown as displaced rectangles (colored) with respect to the black outlines indicating equilibrium positions. The bottom panel shows the corresponding amplitude and phase distributions.